



Article

Improving the Stability of Halide Perovskite Solar Cells Using Nanoparticles of Tungsten Disulfide

Philip Nathaniel Immanuel ^{1,†}, Song-Jeng Huang ^{1,†}, Viktor Danchuk ², Anastasiya Sedova ², Johnathan Prilusky ², Achiad Goldreich ², Hila Shalom ², Albina Musin ³ and Lena Yadgarov ^{2,*}

¹ Department of Mechanical Engineering, National Taiwan University of Science and Technology, Taipei 106, Taiwan

² Department of Chemical Engineering, Faculty of Engineering, Ariel University, Ariel 4076414, Israel

³ Physics Department, Faculty of Natural Sciences, Ariel University, Ariel 4076414, Israel

* Correspondence: lenay@ariel.ac.il

† These authors contributed equally to this work.

Abstract: Halide perovskites-based solar cells are drawing significant attention due to their high efficiency, versatility, and affordable processing. Hence, halide perovskite solar cells have great potential to be commercialized. However, the halide perovskites (HPs) are not stable in an ambient environment. Thus, the instability of the perovskite is an essential issue that needs to be addressed to allow its rapid commercialization. In this work, WS₂ nanoparticles (NPs) are successfully implemented on methylammonium lead iodide (MAPbI₃) based halide perovskite solar cells. The main role of the WS₂ NPs in the halide perovskite solar cells is as stabilizing agent. Here the WS₂ NPs act as heat dissipater and charge transfer channels, thus allowing an effective charge separation. The electron extraction by the WS₂ NPs from the adjacent MAPbI₃ is efficient and results in a higher current density. In addition, the structural analysis of the MAPbI₃ films indicates that the WS₂ NPs act as nucleation sites, thus promoting the formation of larger grains of MAPbI₃. Remarkably, the absorption and shelf life of the MAPbI₃ layers have increased by 1.7 and 4.5-fold, respectively. Our results demonstrate a significant improvement in stability and solar cell characteristics. This paves the way for the long-term stabilization of HPs solar cells by the implementation of WS₂ NPs.

Keywords: methylammonium lead iodide; transition metal dichalcogenides; solar cells; halide perovskite; renewable energy



Citation: Immanuel, P.N.; Huang, S.-J.; Danchuk, V.; Sedova, A.; Prilusky, J.; Goldreich, A.; Shalom, H.; Musin, A.; Yadgarov, L. Improving the Stability of Halide Perovskite Solar Cells Using Nanoparticles of Tungsten Disulfide. *Nanomaterials* **2022**, *12*, 4454. <https://doi.org/10.3390/nano12244454>

Academic Editors: Yi-Je Juang, Yan-Cheng Lin, Li-Hsien Yeh and Yen-Wen Lu

Received: 22 November 2022

Accepted: 9 December 2022

Published: 15 December 2022

Publisher's Note: MDPI stays neutral with regard to jurisdictional claims in published maps and institutional affiliations.



Copyright: © 2022 by the authors. Licensee MDPI, Basel, Switzerland. This article is an open access article distributed under the terms and conditions of the Creative Commons Attribution (CC BY) license (<https://creativecommons.org/licenses/by/4.0/>).

1. Introduction

The ongoing energy crisis, combined with global warming and air pollution, indicates the urgent need to develop cost-effective, environmentally stable and green energy harvest technologies. Solar cells present the most promising paths for green energy harvest in this context. Photovoltaic solar cells are already a part of our life, especially in countries where solar energy is available most of the year. Solar cells make low-cost electricity available for the world's population, particularly for third-world countries. Recently silicon-based solar cells have overtaken the market, but the search for new and more efficient materials is ongoing.

In recent years halide perovskite solar cells (PSCs) have been the center of attention [1–3], reaching an efficiency of 25.7% [4]. This high efficiency and low cost make PSCs great candidates for entering the photovoltaic solar cell market [5]. Halide perovskites (HPs) are very promising due to their high absorption coefficient in the visible region [6], low exciton binding energy [7] and long electron-hole diffusion lengths [8]. The general formula of HPs is ABX₃, where A is usually cesium (Cs) or methylammonium (MA), B is Pb or Sn, and X = I, Br, or Cl [9]. The most commonly studied are methylammonium lead trihalide (CH₃NH₃PbX₃) perovskite with an optical bandgap between 1.5 and 2.3 eV depending on halide type [10,11].

Generally, PSCs are composed of thin layers with different functions for accomplishing four basic processes: (1) absorption of photons with a suitable material, (2) creation of free charge carriers: separation of electron-hole pair by internal field, (3) collection and (4) transportation of photo-generated charge carriers through an electrical circuit (Scheme S1, SI). The n-i-p PSCs architecture commonly involves a planar heterojunction [12] with compact titanium oxide (TiO_2) or tin oxide (SnO_2) as electron transport layers (ETL) [9]. The ETL and the hole transport layer (HTL) assist in separating the electron-hole pairs [1] generated in the perovskite absorber [13].

There are still challenges in fabricating high-performance and stable PSCs for market-oriented fabrication. The principal challenges of PSCs are improving absorption and overcoming the instability caused by moisture, oxygen and heat. One of the possible solutions is adding a transition metal dichalcogenide (TMD) material to improve absorption and stability. TMDs have outstanding stability, ability to conduct both holes and electrons, and high absorption coefficient [14–16].

These two-dimensional (2D) materials consist of an S–M–S sandwich-like structure, where the transition metal atom ($M = \text{W}, \text{Mo}$) are bonded to the chalcogen ($S = \text{S}, \text{Se}, \text{or Te}$) atoms via strong covalent bonds. The MS_2 layers are stacked together by weak van der Waals forces [17,18]. The indirect bandgap of the bulk and multilayer MS_2 converts into a direct one in a single layer [19,20]. Due to a coupling between their mechanical and electrical properties, the semiconducting characteristics of 2D-TMDs are engineered by inducing mechanical, structural, or morphological changes [21–23]. The MoS_2 flakes implemented in the PSCs act as a buffer layer and lead to stable devices. The presence of the MoS_2 suppresses the recombination of electron holes at the HTL/perovskite and ETL/perovskite transport layer interfaces, assists in the charge transfer, and prevents the degradation of the perovskite layer due to the formation of the larger grains [24,25]. In the general PSC scheme, the MoS_2 flakes function mainly as stabilizers and are also used for the transportation of photo-generated charge carriers (fourth basic process). Nevertheless, the exfoliation of MoS_2 flakes from the bulk material is time-consuming and might last up to several days [24–26].

Closed-cage TMDs nanostructures sustain all the properties of the bulk but are much more stable [27,28] due to the lack of dangling bonds and thus can suppress exciton capture at non-radiative recombination centers, such as surface states and impurities. Due to their sizable bandgaps, strongly bound excitons and high oscillator strength, these materials introduce strong light-matter interaction (polaritons) under ambient conditions [27,29–32]. The strong light-matter interaction of WS_2/MoS_2 may further boost the PSCs performance as the plasmonic and polaritonic nanomaterials are often used to boost the efficiency and absorption of the active layers [33]. The polaritons can enhance light absorption, either by electromagnetic field enhancement near the particle or by light scattering into trapped optical modes [34]. In this work, the WS_2 NPs function in the absorption and transportation of photo-generated charges as well. (first and fourth basic processes).

Here, we compare the properties of the absorption layer of the fabricated PSCs with and without the addition of n-type WS_2 NPs, [35,36] and MAPbI_3 . By introducing the WS_2 NPs between the ETL and the active perovskite layer, we obtain a 4.5-fold improvement in the stability of the MAPbI_3 -absorbing layer. Moreover, we observe increased absorption and improved PSCs characteristics upon adding 1 wt% of the WS_2 NPs. The beneficial impact can be explained by the stability and the high absorption coefficient of the WS_2 NP. Another advantage is the overlap between the energy bands, where the upper energy levels of the WS_2 NPs and MAPbI_3 match. This overlap may promote a charge transfer from MAPbI_3 to WS_2 , thus improving charge separation. Moreover, the increase in the absorption of the WS_2 NPs/ MAPbI_3 layers contributes to the generation of electron-hole pairs. We also observe that the WS_2 NPs act as nucleation sites, resulting in larger MAPbI_3 grains, thus hindering nonradiative energy losses. With this study, our results pave the way toward the stabilization of MAPbI_3 -based PSCs.

2. Materials and Methods

2.1. Materials

FTO-covered glass ($6 \Omega/\text{cm}^2$) was purchased from Biotain Hong Kong Co. Limited. Isopropanol (99%) and bi-distilled water (BDW, Milli-Q® IQ 7003) were purchased from Merk, Darmstadt, Germany. Ethanol (99.8%) was purchased from Acros Organics. Chlorobenzene and CH_3NH_3 were purchased from Sigma-Aldrich, USA. Spiro-MeOTAD was purchased from Ossila, Sheffield, UK. Ti-Nanoxide BL/SC was purchased from Solaronix S. A., Switzerland. Ag wire 99.99% was purchased from Advent, UK, PbI_3 (Alfa Aesar, Massachusetts, UK) and used without further purification.

2.2. Solar Cell Fabrication

2.2.1. Fabrication of WS_2 NPs

The multiwall WS_2 NPs are synthesized according to the procedure reported by Tenne et al. [37,38] In detail, on a quartz boat, WO_3 nano-powders (100 nm in dimension) were spread evenly and maintained in a 1% H_2 /99% N_2 gas environment at 900 °C. The WO_3 was reduced to WO_{3-x} (intermediate phases) by the H_2 gas. Following this reaction, the WO_{3-x} was sulfurized by 1% H_2 /99% N_2 and H_2S gas to obtain the fully formed WS_2 NPs.

2.2.2. Fabrication of Solar Cells

For solar cell fabrication, the FTO-covered glass substrates with size $2.5 \text{ cm} \times 2.5 \text{ cm} \times 2.2 \text{ mm}$ are first etched in 3M hydrochloric acid using a special mask of the desired geometry for the electrodes. The etched substrates are then cleaned using an ultrasonic bath (GT Sonic-P3, Guangdong, China) in a cleaning solution (Micro-90 International Products Corporation, USA, diluted with distilled water, 1:50) water-soap solution (2%), distilled water, isopropanol, and deionized water (BDW) for 10 min at 80 °C in each solvent. After each sonication cycle, the substrates are dried with dry air. Then the FTO glass substrates are immersed three times in boiled BDW DI water and dried with nitrogen (N_2). Finally, the FTO substrates are thermally treated at 120 °C for 20 min in a Vacuum Drying Oven DZ-1BC11 (Faithful Inst. Co., China) under 5×10^{-21} Torr pressure. Clean substrates were stored in a desiccator under a vacuum. Before the ETL deposition, the substrates were transferred to a UV-Ozone cleaner for 15–30 min. To cover the FTO substrate with ETL, we drop cast 80 μL Ti-Nanoxide BL/SC (Solaronix, S. A., Switzerland) (TiO_2 , blocking layer) in a static regime, followed by a 30 s spin coating at the speed of 5000 rpm and acceleration of 2500 cycles/ s^2 in the spin coater (WS-650HZ-23NPPB, Laurell Technologies Inc, Lansdale, PA, USA). The FTO/ TiO_2 substrates are then annealed at 550 °C for one hour under continuous dry airflow (600 sccm) in the Tube Furnace KJ-T1200 (Kejia Furnace Co., Ltd., Henan, China).

After 30 s of plasma treatment EQ-PCE3 (MTI Corp., USA) at a “High” regime in residual air at 0.18 torr., 200 μL of WS_2 NPs/ethanol solution (0.07 g/L) was deposited on the FTO/ TiO_2 substrate by spin-coating at the speed of 3000 rpm and then thermally treated in vacuum at 120 °C for 15 min. In the next step, 60 μL MAPbI_3 perovskite precursor solution was applied by spin coating under a controlled N_2 environment in a nitrogen-filled glove box VTI (Vacuum Technology Inc., Oak Ridge, USA) on the formed FTO/ TiO_2 / WS_2 NPs films in an antisolvent strategy [39], modified for double antisolvent treatment. The dots A and B mark the timing of the chlorobenzene (antisolvent) pouring on the top of the forming MAPbI_3 layer, correspondingly 500 and 250 μL . This process produces films of MAPbI_3 with thickness of layer ranging between 300 and 500 nm.

After annealing at 90 °C for 10 min, and cooling to 28 °C, 60 μL of Spiro-MeOTAD was spin-coated at 4000 rpm for 30 sec on the FTO/ TiO_2 / WS_2 NPs/ MAPbI_3 in the dynamic regime. That process produces films of Spiro-MeOTAD with thickness of layer ranging between 300 and 400 nm (Figure S1). In the final step, Ag contact electrodes were deposited by vacuum thermo-resistive evaporation JEE—4B (JEOL, Tokyo, Japan). To avoid Ag atoms' penetration through the HTL layer to the MAPbI_3 causing cell damage, the initial 10 nm of

Ag electrodes were deposited at a rate of 1 nm/min and the remaining 110 nm at a rate of 55 nm/min.

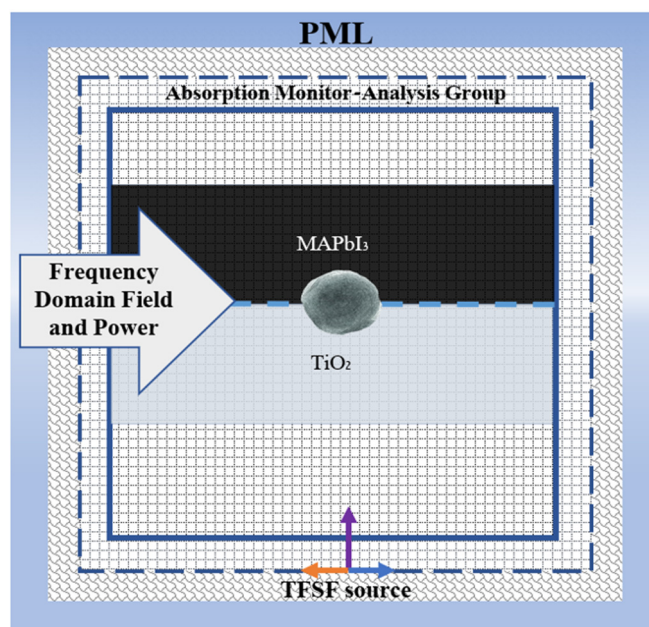
2.3. Characterization

X-ray Diffraction (XRD) patterns are measured using Rigaku SmartLab diffractometer, Tokyo, Japan. The diffractometer is equipped with a Cu anode (CuK α radiation with 1.5418 Å wavelength, 10–80° 2 θ range, step width 0.01°) operated at 40 kV, 120 mA. The scans are acquired in 2-Theta Bragg-Brentano mode. The perovskite films' thickness and surface morphology were revealed with scanning electron microscopy (SEM) MAIA3 (TESCAN, Brno, Czech Republic). The scattering spectra are acquired with Jasco V-750 spectrophotometer in the range of 420 nm to 800 nm. These measurements are used for the band gap calculations. We use a modified Tauc equation to extract the band gap values [40,41].

The PSCs are characterized by a solar simulator (Abet Sun 2000, class A) under standard conditions AM1.5G. The measurements are carried out with an assistance of a Keithley 2400 Sourcemeter (Cleveland, Ohio, United States) and a custom-made program LabView-based. The power conversion efficiency (PCE), short-circuit current density (J_{cs}), open-circuit voltage (V_{OC}) and the fill factor (FF) are calculated from the current density-voltage characteristics (J-V).

2.4. Simulation

Commercial software finite-difference time-domain method (FDTD) (Ansys Lumerical FDTD) was used to perform the simulations [42]. Here, Maxwell's equations are solved in time and space with various mesh sizes. A broadband Total-Field Scattered-Field (TFSF) source is used in the wavelength domain (400–800 nm) to measure the local electric field. The electric field response from the materials is captured using a 2D monitor. The frequency domain field and power monitor directly measure the local field enhancement. The cross-section of the simulation scheme is presented in Scheme 1.



Scheme 1. Cross section view of the simulation system.

The embedded WS₂ NP at the interface of TiO₂ and MAPbI₃ is modeled as a sphere inside a dielectric material. The model, without the WS₂ NP, is considered the reference model and the signal is considered as the reference signal. We examine the size effect of the WS₂ nanoparticle (10–80 nm). The background index of the FDTD region was set to be $n = 1$ for air. The dielectric functions of MAPbI₃, TiO₂, and WS₂ are extracted from [43–45]

In this simulation system, the mesh order of the NP was set to 2, and the TiO_2 and MAPbI_3 mesh orders were 3 [46].

2.5. Stability Measurements

We studied the stability of the MAPbI_3 layers with and without WS_2 NPs by exposing the sample to light and ambient environment. The WS_2 NP and MAPbI_3 thin layers were produced using the procedure described for solar cell in Section 2.2.2. Several stability tests were performed. (1) The MAPbI_3 layers on top of the FTO glass with and without WS_2 NPs were exposed to air for one hour and sealed and stored in a vacuum standard vacuum drawer for one month. (2) Here, the examined materials were placed on the glass, not on FTO. All the samples were vacuum sealed in a petri dish and kept under sunlight for 11 days. (3) The samples were vacuum sealed in a plastic bag and exposed to sunlight. The reflection of all the samples from test 2 and 3 was measured every few days and the samples were re-sealed under vacuum. For test 1, the samples were photographed after one month. To analyze the results, the reflection of samples from tests 2 and 3 were converted to absorption using the following formula $A = 1 - R$, where A stand for the absorption and R denotes the reflection. The measured spectra are presented in Figures S2a,b and S3a–c. For all the measured spectra the intensity at 700 nm was chosen for the absorption intensity comparison of the samples.

Additionally, the performance of the PSCs was examined in two other configurations by placing the WS_2 NPs (1) into the MAPbI_3 precursor and (2) in between the HTL and MAPbI_3 . Here, the results were very inconclusive and thus not presented in this work.

3. Results and Discussion

The morphology of the WS_2 NPs was studied by SEM and TEM, as shown in Figure 1a,b. The average dimension of the NPs is in the range of ~60 to 120 nm in diameter. [28] The closed cage WS_2 hollow nanoparticles appear to be crystalline and faceted. The absorption spectrum of the WS_2 NPs has two peaks at 630 and 530 nm, as shown in Figure 1c. These two peaks are due to the two excitonic transitions in WS_2 NPs [28].

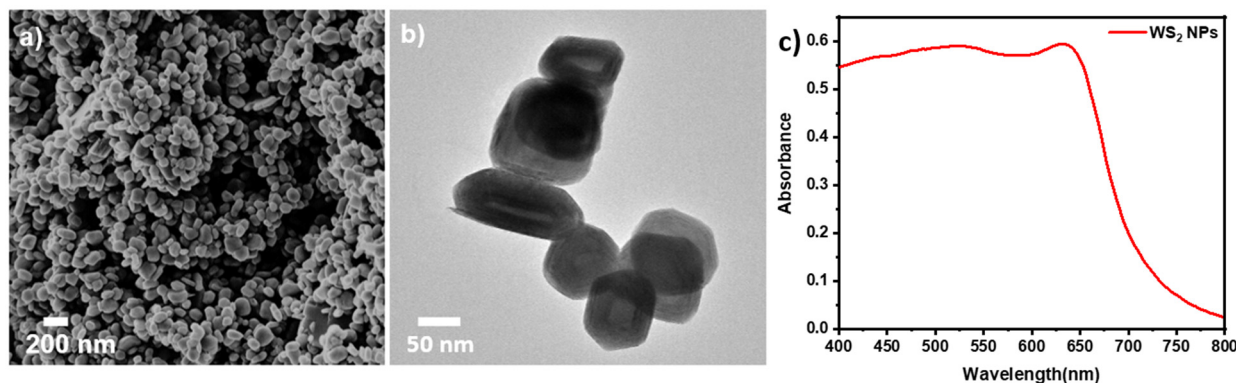


Figure 1. (a) SEM image of WS_2 NPs, (b) TEM image of WS_2 NPs. (c) absorption spectrum of WS_2 NPs.

To investigate the influence of WS_2 NPs on MAPbI_3 films, the morphological changes, and the crystalline phase of the films was studied by SEM and XRD, respectively. The SEM images of MAPbI_3 and WS_2 NPs/ MAPbI_3 films are shown in Figure 2a,b. The average grain size of the pristine MAPbI_3 layer is smaller (247.48 ± 56.28 nm) and narrow in distribution (Figure S4a). However, the MAPbI_3 deposited on top of the WS_2 NPs has large grains and wide distribution (271.17 ± 55.44 nm) (Figure S4b). These results indicate that adding WS_2 NPs increases the MAPbI_3 grain size. Moreover, the absorbance of the HPs is enhanced due to the high absorption coefficient of the WS_2 NPs ($1 \times 10^6 \text{ cm}^{-1}$) [47]. The WS_2 NPs contributes to increased absorption, as well as the enlarged grain size, which leads to enhanced photocurrent [48]. The absorption of photons causes electrons(e-) to

eject and produce photocurrent. When the absorbance is enhanced, more photons will be absorbed and more electrons will be ejected, which results in a high photocurrent. Thus, the absorption enhances the photocurrent. [48] The XRD results (Figure 2c) show that the formed MAPbI₃ film with and without the WS₂ NPs contains ~99.5% of the tetragonal MAPbI₃ phase [49,50]. The close analysis of the diffraction patterns reveals only a minute amount (~0.5%) of the monoclinic lead iodide phase. That phase is present in the thin MAPbI₃ layer due to the incomplete conversion to the perovskite phase [51].

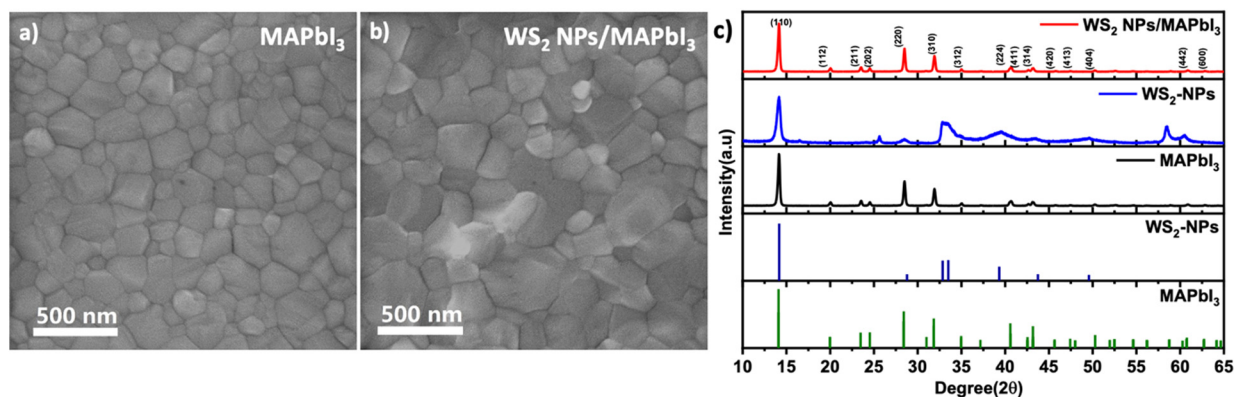


Figure 2. (a) SEM image of MAPbI₃, (b) SEM image of WS₂ NPs/MAPbI₃, and (c) XRD patterns of the MAPbI₃, WS₂ NPs, and WS₂ NPs/MAPbI₃.

To understand the effect on grain size and crystalline phases and to find the optimal concentration of WS₂ NPs, the MAPbI₃ films were prepared with different weight percentages (wt%) of WS₂ NPs (1%, 2%, and 3%). The morphology and the phase were examined by SEM and XRD (Figures S5a–c and S6), respectively. Interestingly, the XRD spectra show no indication of WS₂ NPs presence in the MAPbI₃ films, even upon increasing the WS₂ NPs concentration (Figure S6). This can be assigned to the overlap between the (110) and (002) peaks of MAPbI₃ and WS₂ NPs, respectively. Due to the low WS₂ NPs concentration, the lower intensity peaks of WS₂ are hidden in the MAPbI₃ spectral background. According to SEM analysis, there is no significant difference in the grain size (268.58 ± 63.20) between the 1 wt% and when the WS₂ NPs concentration was double (2 wt%) (Figure S5d). When the concentration tripled, the average grain size became smaller (200.41 ± 69.6 nm). The changes in the grain size can be explained by the aggregation of the NPs. Namely, when the concentration of the WS₂ NPs was higher than 1 wt%, more NPs aggregate form and act as multiple nucleation centers. The increase in the number of the formed aggregates is further verified by SEM analysis of the WS₂ NPs deposited on a substrate with different concentrations (1 and 3 wt%) (Figure S7a,b). The combination of SEM and XRD analysis indicates that adding 1 wt% of WS₂ NPs to the MAPbI₃ films produces larger grains of the latter without changing its phase. The larger grain size has a beneficial impact on the absorption, stability and efficiency of the PSCs [25,52,53]. Moreover, it reduces the number of grain boundaries and thus decreases the non-radiative processes [48], and enhances the absorption and photocurrent [48]. Hence, for further experiments and characterization, we use 1 wt% of WS₂ NPs to prepare MAPbI₃ films and PSCs.

To study the optical properties of the hybrid system, the reflectance of the pristine MAPbI₃ films and WS₂ NPs/MAPbI₃ were examined. Impressively, the measured reflectance shows a 1.7-fold reduction in the reflectance upon the addition of 1 wt% of WS₂ NPs. (Figure 3a) These results indicate that the WS₂ NPs/MAPbI₃ layers absorb much more photons compared to the pristine MAPbI₃. Importantly, the low content of the added WS₂ NPs increases the absorbance but does not affect the band gap of the MAPbI₃ (Figure S8). Here, the band gap of both hybrid and pristine films is 1.63 eV, which is characteristic of MAPbI₃ [10].

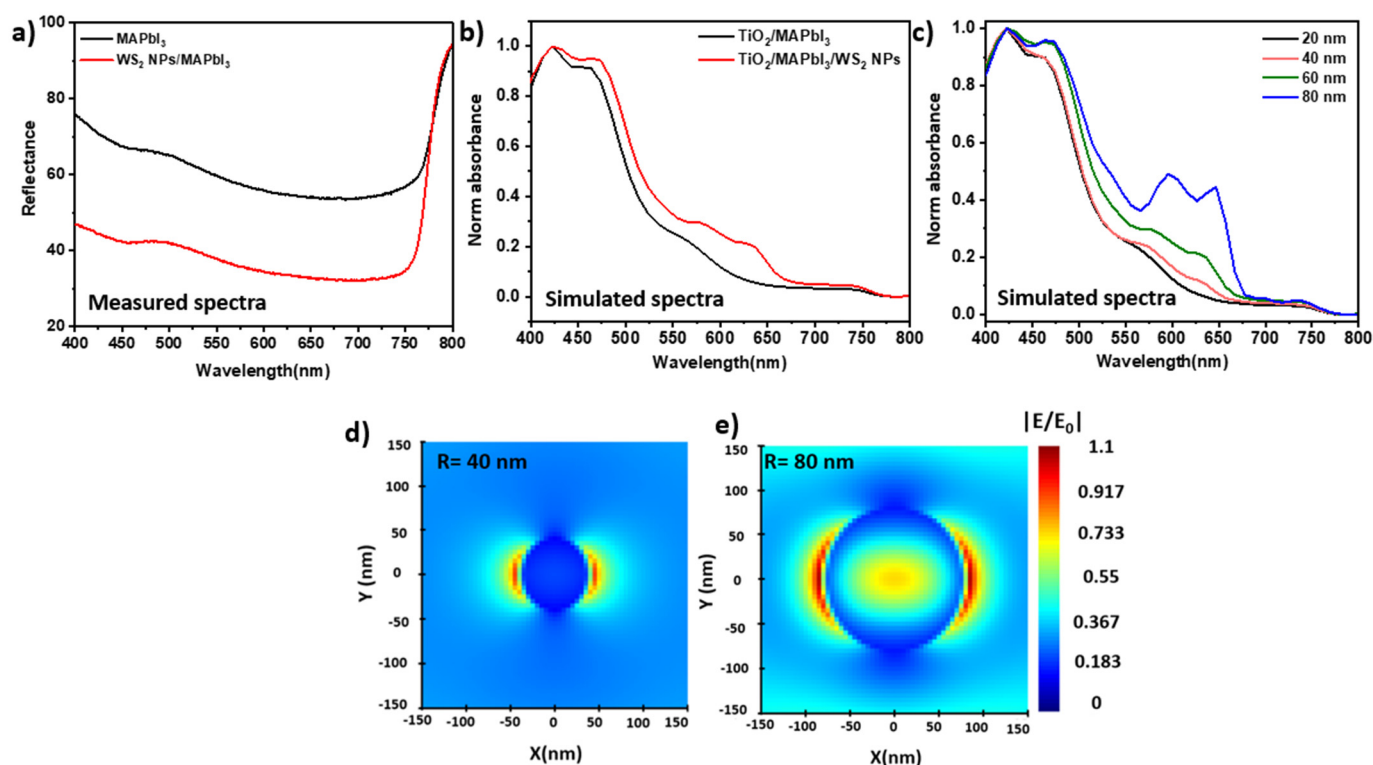


Figure 3. (a) Reflectance spectrum of MAPbI₃ and WS₂ NPs/MAPbI₃, (b) simulated absorption spectrum of MAPbI₃/WS₂ NPs and MAPbI₃/WS₂ NPs/TiO₂, (c) simulated absorption spectrum of WS₂ NPs with different radius, (d,e) simulated electric field distribution at 710 nm of WS₂ NPs with radius of (d) 40 nm (e) 80 nm.

To understand the impact of particle size and concentration of the WS₂ NPs on absorbance, we simulate the absorption spectra of the MAPbI₃ and WS₂ NPs/MAPbI₃ on TiO₂ substrate (120 nm). The simulations were performed using commercial software: Ansys Lumerical FDTD [54–56]. The TiO₂ substrate was chosen to consider the relevant contribution of the relevant interfaces, namely the ETL and the absorbing layer (MAPbI₃). The absorption spectra of MAPbI₃ on TiO₂ with and without WS₂ NPs are presented in Figure 3b. The additional peaks at 550 nm to 720 nm (red line) are due to the contribution of WS₂ NPs to the MAPbI₃ absorbance. The simulation results further support the experimental observations. Here again, the absorption of the MAPbI₃ film increases upon the addition of the WS₂ NPs. Nevertheless, a substantial difference between the experimental and the simulated spectra are clearly observed. One of the reasons is the substrate. Namely, the measured film is placed on the glass, where the simulated film is located on TiO₂. The experimental measurement was on a glass substrate, but the simulation was performed with the background of TiO₂. An additional reason is a difference in the measurement setup: standard spectrophotometer vs. perfect simulation conditions. Notwithstanding, the simulation results manifest the beneficial impact of WS₂ NPs on the increased absorbance of the MAPbI₃ films.

Additionally, we simulated the absorption of the WS₂ NPs with different radii to study the impact of dimension and concentration on the enhancement factor (Figure 3c–e). The absorption intensity increases with the radius of the WS₂ NPs (Figure 3c). Furthermore, the electric field ($|E/E_0|^2$) of the larger WS₂ NP ($d = 80$ nm) is much broader and more intense compared to the one of $d = 40$ nm. The absorption intensity and the $|E/E_0|^2$ fields are higher for the larger NPs, which is beneficial for PSCs performance.

Next, we study the influence of WS₂ NPs on the stability of MAPbI₃ films by examining the latter in a vacuum and under sunlight. For the preliminary stability test, the MAPbI₃ layers on FTO glass with and without the WS₂ NPs were examined. The

MAPbI₃ layers were exposed to air for one hour, then sealed and stored in darkness for one month. The microscope images of the MAPbI₃ and WS₂ NPs/MAPbI₃ are presented in Figure S9. Impressively, the MAPbI₃ layers appear with cracks (Figure 4a), while the WS₂ NPs/MAPbI₃ layers remain undamaged (Figure 4b). These results demonstrate positive long-term stability effects of the WS₂ NPs on the MAPbI₃ films.

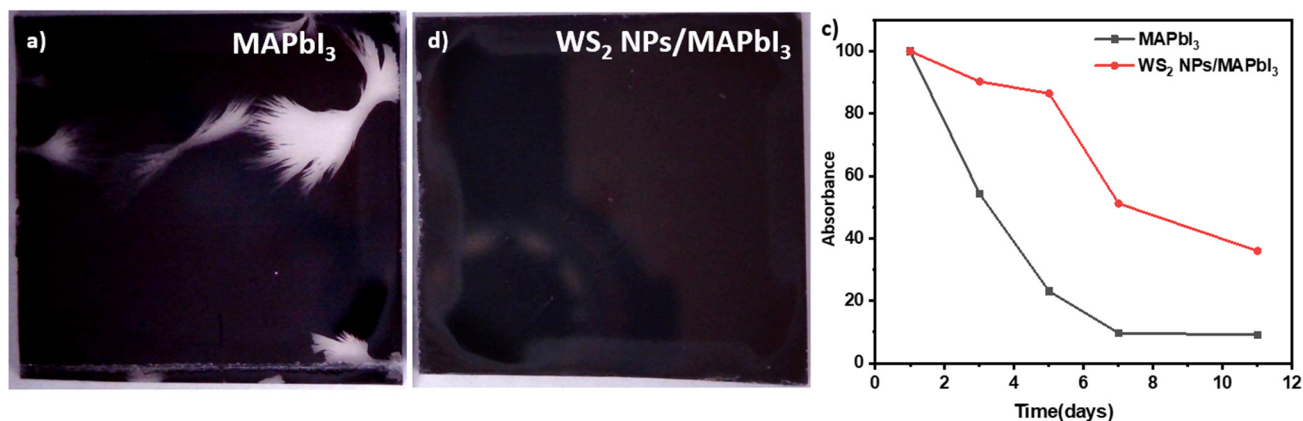


Figure 4. (a) MAPbI₃ and (b) WS₂ NPs/MAPbI₃ layers on top of the FTO glass substrate after exposure to air, (c) stability measurement of the samples: the absorption percentage of the hybrid WS₂ NPs/MAPbI₃ (red line) and the pristine MAPbI₃ (black line).

Following the successful preliminary results, the long-term stability of WS₂ NPs/MAPbI₃ and MAPbI₃ films under sunlight in a vacuum was examined. The samples were placed in a petri dish, vacuum sealed and exposed to sunlight for eleven days. The absorption of the films was measured every few days (Figures S3a,b and S10). Figure 4c shows the comparison between the absorption percentage of the hybrid WS₂ NPs/MAPbI₃ and the pristine MAPbI₃. The absorption of both films decreases upon exposure to sunlight. However, while the absorption of MAPbI₃ film decreased by almost 50% in the first 3 days, the absorption of the hybrid film decreases only by 10%. This trend proceeds and the absorption of the MAPbI₃ film decreases by 90% of the initial intensity in seven days. Outstandingly, the absorption of the WS₂ NPs/MAPbI₃ films remains high and starts to drop only after 5 days. Moreover, on the eleventh day, the absorption percentage of the hybrid was as high as 40% whereas the absorption of MAPbI₃ film was only 10%. These excellent results indicate that a minute amount of WS₂ NPs dramatically stabilizes the MAPbI₃. Additionally, we examined the stability of the MAPbI₃ and WS₂ NPs/MAPbI₃ film in a vacuum sealed bag under sunlight, and the results are presented in Figure S3a–c. Here again, the hybrid films exhibit better stability compared to the pristine ones (MAPbI₃). The phenomenon's proposed mechanism includes charge separation [57] and heat dissipation [58]. The WS₂ thermal conductivity is high, so it dissipates heat rapidly. Furthermore, the charge separation occurred in the HPs by transferring the photoexcited charges to WS₂ NPs [57,59]. The observed stabilization impact of a minute amount of WS₂ on MAPbI₃ films is extraordinary. Namely, 1 wt% of WS₂ NPs is sufficient to stabilize the WS₂ NPs/MAPbI₃ films by 4.5-fold.

Finally, the WS₂/PSCs performance was examined using the J-V characteristics. The Figure 5a illustrate a schematic representation of the WS₂ NPs/MAPbI₃-based PSCs, where MAPbI₃ is deposited on top of the WS₂ NPs. In this configuration, the formed MAPbI₃ layer is in contact with the n-type separation [35,36] and with TiO₂ ETL. According to the energy levels diagram of the formed layers in Figure 5b, [23,60,61] the upper energy levels of the MAPbI₃ and WS₂ NPs are practically matching. This energetic match allows a fast electron transition from the MAPbI₃ to the n-type WS₂ NPs. [59] Moreover, the hole diffusion is most likely heading from WS₂ NPs to the MAPbI₃ and to the Spiro-OMeTAD polymer.

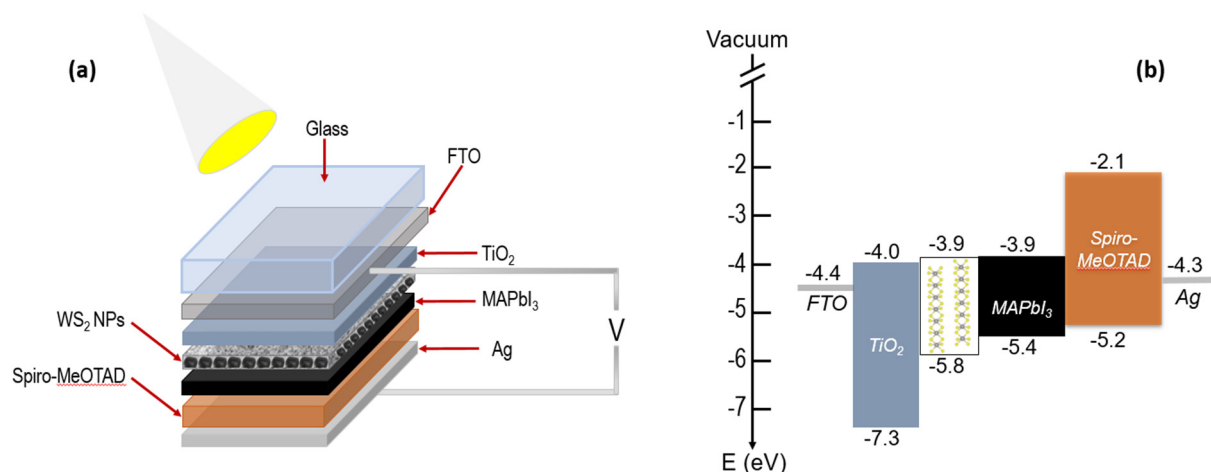


Figure 5. (a) configuration of WS_2 NPs/ MAPbI_3 heterostructure-based PSCs, and (b) schematic energy level diagram.

We analyze the performance of the PSCs with the absorbing layer of MAPbI_3 and compare it with WS_2 NPs/ MAPbI_3 . Here the vastly studied MAPbI_3 -based PSC serves as a reference cell. The measured values are somewhat low compared to the results presented in the literature [25,62]. This can be explained by using an unstable hole transport layer and non-optimal experimental conditions. In the future, the photovoltaic parameters of our devices can be boosted by replacing the Ag contacts with gold (Au) or platinum (Pt) [63]. The PSCs might also be improved by refining the conditions, such as using a more efficient and stable hole transport layer and electron transport layer. The characteristic performance for three PSCs was measured on selective days and the average values are presented in Figure 6. Moreover, compared to the reference, the hybrid samples exhibited higher values of the V_{OC} , FF, J_{SC} , and, as a result, PCE (Table 1). The difference is 5.9% and 59.63% for the V_{OC} and PCE, respectively (Figure 6a–c).

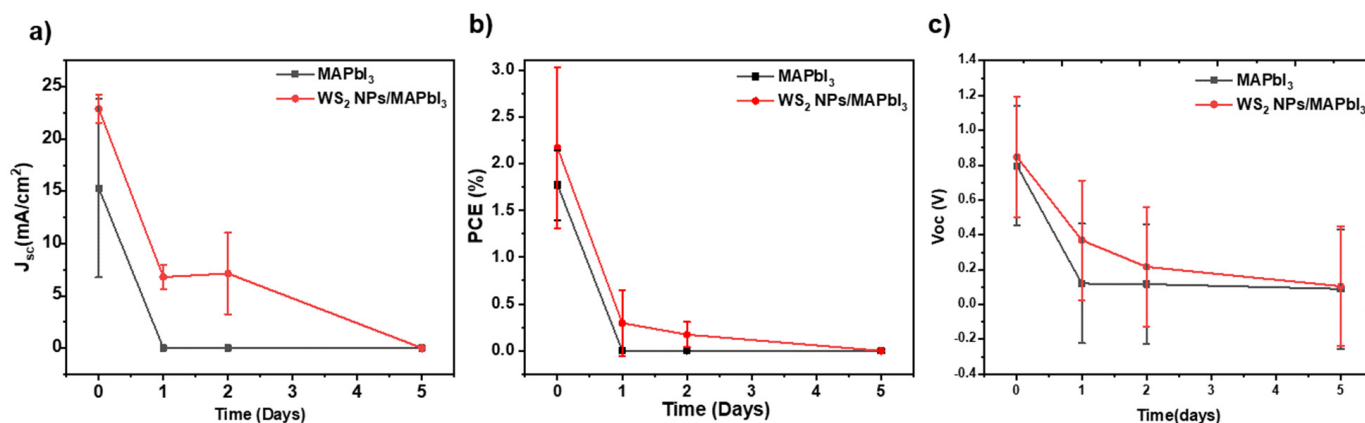


Figure 6. (a) J–V characteristic, (b) PCE and (c) V_{OC} of MAPbI_3 and WS_2 NPs/ MAPbI_3 PSCs for different days.

Table 1. Photovoltaic parameters of the devices without (MAPbI_3) and with WS_2 NPs (WS_2 NPs/ MAPbI_3).

Device	V_{OC} (V)	J_{SC} (mA · cm ^{−2})	FF (%)	PCE (%)
MAPbI_3	0.79 ± 0.3	15.30 ± 8.54	14.88	1.34 ± 0.29
WS_2 NPs/ MAPbI_3	0.84 ± 0.3	22.89 ± 1.35	16.85	3.32 ± 0.61
Difference (%)	5.9%	33.1%	11%	59.63%

Interestingly, we see that the J_{SC} tends to be higher for the cells with WS_2 NPs/ $MAPbI_3$, supporting the idea of the efficient electron transfer from the $MAPbI_3$ to WS_2 NPs. Similar results are reported for the MoS_2 buffer layer that assists in the transition of holes from $MAPbI_3$ to Spiro-OMeTAD and the stabilization of the PSCs [24]. One of the disadvantages of the MoS_2 flakes implementation is the time-consuming process of their exfoliation from the bulk material. The time of this process ranges from 6 to 66 h, thus substantially increasing the time for fabrication of the PSCs devices [24–26]. Here, we solve this problem by using the WS_2 NPs that can be incorporated as received. Moreover, the closed cage nanostructures are much more stable than the layered counterparts due to the fewer defects and lack of dangling bonds in the latter.

4. Conclusions

We demonstrate a conceptual study where we suggest using the WS_2 NPs as an additive to the absorbing layer for improved stability and absorption of PSCs. Here, the WS_2 NPs are used as a charge separation layer in the $MAPbI_3$ -based PSCs with compact TiO_2 . These NPs can be incorporated as is and without any treatment, giving an advantage over the studies reported on MoS_2 flakes to date. The results of our studies indicate that adding a minute amount of WS_2 NPs increases the $MAPbI_3$ grain size and enhances the overall absorbance, which leads to enhanced photocurrent. The simulation results show that the absorption is high for bigger NPs, which favors enhancing the absorption of the $MAPbI_3$ layers. The high concentration of WS_2 NPs leads to produce small grains due to aggregation, although the minute amount (1 wt%) of the WS_2 NPs used for the PSCs devices produces larger grains and enhances the stability of $MAPbI_3$ layers by 4.5-fold. These preliminary results show a clear potential for the use of WS_2 NPs in the long-term stabilization of the PSCs.

Supplementary Materials: The following supporting information can be downloaded at: <https://www.mdpi.com/article/10.3390/nano12244454/s1>, Scheme S1. (a) absorption of photons with WS_2 NPs/ $MAPbI_3$, (b) creation of free charge carriers: separation of electron-hole pair by internal field, (c) collection and (d) transportation of photo-generated charge carriers through an electrical circuit. Figure S1. Cross section SEM images of $MAPbI_3$ layer. Figure S2. Stability measurement of (a) $MAPbI_3$ and (b) WS_2 NPs/ $MAPbI_3$ films in petri dish. Figure S3. Stability measurement of (a) $MAPbI_3$, (b) WS_2 NPs/ $MAPbI_3$ films on vacuum sealed bags, (c) absorption percentage of the hybrid WS_2 NPs/ $MAPbI_3$ (red line) and the pristine $MAPbI_3$ (black line). Figure S4. Grain size distribution of (a) $MAPbI_3$ and (b) WS_2 NPs/ $MAPbI_3$ with 1 wt%. Figure S5. (a–c) SEM images of the WS_2 NPs/ $MAPbI_3$ layers with increased concentration of WS_2 NPs. Here C1—1 wt% concentration of WS_2 NPs, C2—2 wt% concentration of WS_2 NPs, C3—3 wt% concentration of WS_2 NPs. (d) Grain size distribution of (a) WS_2 NPs/ $MAPbI_3$ for C2 concentration of NPs and (e) WS_2 NPs/ $MAPbI_3$ for C3 concentration of NPs. (f) Absorbance spectrum of $MAPbI_3$ with three grain size. Figure S6. XRD patterns of the WS_2 NPs/ $MAPbI_3$ layers with increased concentration of WS_2 NPs. Here C1—1 wt% concentration of WS_2 NPs, C2—2 wt% concentration of WS_2 NPs, C3—3 wt% concentration of WS_2 . Figure S7. (a) SEM images of WS_2 NPs on glasses with C1 concentration and (b) SEM images of WS_2 NPs on glasses with C3 concentration. Figure S8. Calculated band gap of $MAPbI_3$ and WS_2 NPs/ $MAPbI_3$. Figure S9. Light microscope images of three different magnifications of the (a–c) $MAPbI_3$ and (d–f) WS_2 NPs/ $MAPbI_3$ layers on the FTO glass after exposure to air. Figure S10. Picture of $MAPbI_3$ films and WS_2 NPs/ $MAPbI_3$ films after stability test under sun light.

Author Contributions: Conceptualization, methodology, L.Y. and V.D.; software, J.P.; validation, L.Y. and A.S.; Formal analysis, H.S.; investigation, L.Y.; resources, data curation, A.G. and H.S.; writing—original draft preparation, P.N.I. and A.S.; writing—review and editing, P.N.I., L.Y. and S.-J.H.; visualization, A.S., P.N.I. and H.S.; supervision, L.Y.; project administration, L.Y. and A.M.; All authors have read and agreed to the published version of the manuscript.

Funding: We acknowledge financial support from the Ministry of Energy, Israel, through their support of this research under contract number: 221-11-042.

Institutional Review Board Statement: Not applicable.

Informed Consent Statement: Not applicable.

Conflicts of Interest: The authors declare no conflict of interest.

References

- Jung, H.S.; Park, N.G. Perovskite solar cells: From materials to devices. *Small* **2015**, *11*, 10–25. [CrossRef] [PubMed]
- Correa-Baena, J.; Saliba, M.; Buonassisi, T.; Grätzel, M.; Abate, A.; Tress, W.; Hagfeldt, A. Promises and challenges of perovskite solar cells. *Science* **2017**, *358*, 739–744. [CrossRef] [PubMed]
- Zheng, J.; Mehrvarz, H.; Ma, F.; Lau, C.; Green, M.; Huang, S.; Ho-baillie, A. 21.8% Efficient Monolithic Perovskite/Homo-Junction-Silicon Tandem Solar Cell on 16 cm². *ACS Energy Lett.* **2018**, *3*, 2299–2300. [CrossRef]
- National Renewable Energy Laboratory (NREL). Available online: <https://www.nrel.gov/pv/cell-efficiency.html> (accessed on 29 November 2022).
- Snaith, H.J. Perovskites: The emergence of a new era for low-cost, high-efficiency solar cells. *J. Phys. Chem. Lett.* **2013**, *4*, 3623–3630. [CrossRef]
- Green, M.A.; Ho-Baillie, A.; Snaith, H.J. The emergence of perovskite solar cells. *Nat. Photonics* **2014**, *8*, 506–514. [CrossRef]
- Miyata, A.; Mitioglu, A.; Plochocka, P.; Portugall, O.; Wang, J.T.; Stranks, S.D.; Snaith, H.J.; Nicholas, R.J. Direct measurement of the exciton binding energy and effective masses for charge carriers in organic–inorganic tri-halide perovskites. *Nat. Phys.* **2015**, *11*, 582–587. [CrossRef]
- Stranks, S.D.; Eperon, G.E.; Grancini, G.; Menelaou, C.; Alcocer, M.J.P.; Leijtens, T.; Herz, L.M.; Petrozza, A.; Snaith, H.J. Electron-hole diffusion lengths exceeding 1 micrometer in an organometal trihalide perovskite absorber. *Science* **2013**, *342*, 341–344. [CrossRef]
- Ajena, K.; Kulkarni, A.; Miyasaka, T. Halide perovskite photovoltaics: Background, status, and future prospects. *Chem. Rev.* **2019**, *119*, 3036–3103.
- Amat, A.; Mosconi, E.; Ronca, E.; Quarti, C.; Umari, P.; Nazeeruddin, M.K.; Grätzel, M.; de Angelis, F. Cation-induced band-gap tuning in organohalide perovskites: Interplay of spin-orbit coupling and octahedra tilting. *Nanotechnol. Lett.* **2014**, *14*, 3608–3616. [CrossRef]
- Sadhukhan, P.; Das, S. Photo detector based on graded band gap perovskite crystal. *Sol. Energy* **2019**, *194*, 563–568. [CrossRef]
- Liu, M.; Johnston, M.B.; Snaith, H.J. Efficient planar heterojunction perovskite solar cells by vapour deposition. *Nature* **2013**, *501*, 395–398. [CrossRef] [PubMed]
- Kim, H.; Lee, C.; Im, J.; Lee, K.; Moehl, T.; Marchioro, A.; Moon, S.; Humphry-Baker, R.; Yum, J.; Moser, J.E.; et al. Lead iodide perovskite sensitized all-solid-state submicron thin film mesoscopic solar cell with efficiency exceeding 9%. *Sci. Rep.* **2012**, *2*, 1–7. [CrossRef] [PubMed]
- Ovchinnikov, D.; Allain, A.; Huang, Y.S.; Dumcenco, D.; Kis, A. Electrical transport properties of single-layer WS₂. *ACS Nanotechnol.* **2014**, *8*, 8174–8181. [CrossRef]
- Zhang, Y.; Ye, J.; Matsushashi, Y.; Iwasa, Y. Ambipolar MoS₂ thin flake transistors. *Nanotechnol. Lett.* **2012**, *12*, 1136–1140. [CrossRef] [PubMed]
- Radisavljevic, B.; Radenovic, A.; Brivio, J.; Giacometti, V.; Kis, A. Single-layer MoS₂ transistors. *Nat. Nanotechnol.* **2011**, *6*, 147–150. [CrossRef] [PubMed]
- Wang, Q.H.; Kalantar-Zadeh, K.; Kis, A.; Coleman, J.N.; Strano, M.S. Electronics and optoelectronics of two-dimensional transition metal dichalcogenides. *Nat. Nanotechnol.* **2012**, *7*, 699–712. [CrossRef]
- Yuwen, L.; Xu, F.; Xue, B.; Luo, Z.; Zhang, Q.; Bao, B.; Su, S.; Weng, L.; Huang, W.; Wang, L. General synthesis of noble metal (Au, Ag, Pd, Pt) nanocrystal modified MoS₂ nanosheets and the enhanced catalytic activity of Pd–MoS₂ for methanol oxidation. *Nanoscale* **2014**, *6*, 5762–5769. [CrossRef]
- Mak, K.F.; Lee, C.; Hone, J.; Shan, J.; Heinz, T.F. Atomically thin MoS₂: A new direct-gap semiconductor. *Phys. Rev. Lett.* **2010**, *105*, 136805. [CrossRef]
- Splendiani, A.; Sun, L.; Zhang, Y.; Li, T.; Kim, J.; Chim, C.; Galli, G.; Wang, F. Emerging photoluminescence in monolayer MoS₂. *Nanotechnol. Lett.* **2010**, *10*, 1271–1275. [CrossRef]
- Jiang, J.-W.; Qi, Z.; Park, H.S.; Rabczuk, T. Elastic bending modulus of single-layer molybdenum disulfide (MoS₂): Finite thickness effect. *Nanotechnology* **2013**, *24*, 435705. [CrossRef]
- Allan, D.R.; Kelsey, A.A.; Clark, S.J.; Angel, R.J.; Ackland, G.J. High-pressure semiconductor-semimetal transition in TiS₂. *Phys. Rev. B* **1998**, *57*, 5106. [CrossRef]
- Ghosh, S.; Brüser, V.; Kaplan-Ashiri, I.; Popovitz-Biro, R.; Peglow, S.; Martínez, J.I.; Alonso, J.A.; Zak, A. Cathodoluminescence in single and multiwall WS₂ nanotubes: Evidence for quantum confinement and strain effect. *Appl. Phys. Rev.* **2020**, *7*, 41401. [CrossRef]
- Capasso, A.; Matteocci, F.; Najafi, L.; Prato, M.; Buha, J.; Cinà, L.; Pellegrini, V.; di Carlo, A.; Bonaccorso, F. Few-layer MoS₂ flakes as active buffer layer for stable perovskite solar cells. *Adv. Energy Mater.* **2016**, *6*, 1600920.
- Liua, Z.; Liu, K.; Zhang, F.; Jain, S.M.; He, T.; Jiang, Y.; Liu, P.; Yang, J.; Liu, H.; Yuan, M. CH₃NH₃PbI₃:MoS₂ heterostructure for stable and efficient inverted perovskite solar cell. *Sol. Energy* **2020**, *195*, 436–445. [CrossRef]

26. Ahmed, M.I.; Hussain, Z.; Khalid, A.; Amin, H.M.N.; Habib, A. Absorption enhancement in $\text{CH}_3\text{NH}_3\text{PbI}_3$ solar cell using a $\text{TiO}_2/\text{MoS}_2$ nanocomposite electron selective contact. *Mater. Res. Express* **2016**, *3*, 45022. [CrossRef]
27. Yadgarov, L.; Višić, B.; Abir, T.; Tenne, R.; Polyakov, A.Y.; Levi, R.; Dolgova, T.V.; Zubuyuk, V.V.; Fedyanin, A.A.; Goodilin, E.A. Strong light-matter interaction in tungsten disulfide nanotubes. *Phys. Chem. Chem. Phys.* **2018**, *20*, 20812–20820. [CrossRef]
28. Sinha, S.S.; Višić, B.; Byregowda, A.; Yadgarov, L. Dynamical Nature of Exciton-Polariton Coupling in WS_2 Nanoparticles. *Isr. J. Chem.* **2022**. [CrossRef]
29. Sinha, S.S.; Zak, A.; Rosentsveig, R.; Pinkas, I.; Tenne, R.; Yadgarov, L. Size-Dependent Control of Exciton-Polariton Interactions in WS_2 Nanotubes. *Small* **2020**, *16*, 1–10. [CrossRef]
30. Višić, B.; Yadgarov, L.; Pogna, E.A.A.; Conte, S.D.; Vega-Mayoral, V.; Vella, D.; Tenne, R.; Cerullo, G.; Gadermaier, C. Ultrafast nonequilibrium dynamics of strongly coupled resonances in the intrinsic cavity of WS_2 nanotubes. *Phys. Rev. Res.* **2019**, *1*, 033046. [CrossRef]
31. Sinha, S.S.; Yadgarov, L.; Aliev, S.B.; Feldman, Y.; Pinkas, I.; Chithaiah, P.; Ghosh, S.; Idelevich, A.; Zak, A.; Tenne, R. MoS_2 and WS_2 Nanotubes: Synthesis, Structural Elucidation, and Optical Characterization. *J. Phys. Chem. C* **2021**, *125*, 6324–6340. [CrossRef]
32. Verre, R.; Baranov, D.G.; Munkhbat, B.; Cuadra, J.; Käll, M.; Shegai, T. Transition metal dichalcogenide nanodisks as high-index dielectric Mie nanoresonators. *Nat. Nanotechnol.* **2019**, *14*, 679–683. [CrossRef] [PubMed]
33. Ferry, V.E.; Munday, J.N.; Atwater, H.A. Design considerations for plasmonic photovoltaics. *Adv. Mat.* **2010**, *22*, 4794–4808. [CrossRef] [PubMed]
34. Jang, Y.H.; Jang, Y.J.; Kim, S.; Quan, L.N.; Chung, K.; Kim, D.H. Plasmonic Solar Cells: From Rational Design to Mechanism Overview. *Chem. Rev.* **2016**, *116*, 14982–15034. [CrossRef] [PubMed]
35. Levi, R.; Bitton, O.; Leitun, G.; Tenne, R.; Joselevich, E. Field-effect transistors based on WS_2 nanotubes with high current-carrying capacity. *Nanotechnol. Lett.* **2013**, *13*, 3736–3741. [CrossRef]
36. Macchia, E.; Zak, A.; Picca, R.A.; Manoli, K.; di Franco, C.; Cioffi, N.; Scamarcio, G.; Tenne, R.; Torsi, L. improved performance p-type polymer (P_3HT)/n-type nanotubes (WS_2) electrolyte gated thin-film transistor. *MRS Adv.* **2018**, *3*, 1525–1533. [CrossRef]
37. Rothschild, A.; Sloan, J.; Tenne, R. Growth of WS_2 nanotubes phases. *J. Am. Chem. Soc.* **2000**, *122*, 5169–5179. [CrossRef]
38. Chithaiah, P.; Ghosh, S.; Idelevich, A.; Rovinsky, L.; Livneh, T.; Zak, A. Solving the ‘ MoS_2 Nanotubes’ Synthetic Enigma and Elucidating the Route for Their Catalyst-Free and Scalable Production. *ACS Nanotechnol.* **2020**, *14*, 3004–3016. [CrossRef]
39. Saliba, M.; Matsui, T.; Domanski, K.; Seo, J.; Ummadisingu, A.; Zakeeruddin, S.M.; Correa-Baena, J.; Tress, W.R.; Abate, A.; Hagfeldt, A. Incorporation of rubidium cations into perovskite solar cells improves photovoltaic performance. *Science* **2016**, *354*, 206–209. [CrossRef]
40. Tauc, J.; Grigorovici, R.; Vancu, A. Optical properties and electronic structure of amorphous germanium. *Phys. Status Solidi* **1966**, *15*, 627–637. [CrossRef]
41. Makula, P.; Pacia, M.; Macyk, W. How to correctly determine the band gap energy of modified semiconductor photocatalysts based on UV-Vis spectra. *ACS Publ.* **2018**, *9*, 6814–6817. [CrossRef]
42. Lumerical inc.FDTD:3D Electromagnetic Simulator; Vancouver, Canada. Available online: <https://www.ansys.com/products/photonics/dgtd> (accessed on 1 December 2022).
43. Kato, M.; Fujiseki, T.; Miyadera, T.; Sugita, T.; Fujimoto, S.; Tamakoshi, M.; Chikamatsu, M.; Fujiwara, H. Universal rules for visible-light absorption in hybrid perovskite materials. *J. Appl. Phys.* **2017**, *121*, 115501. [CrossRef]
44. Kischkat, J.; Peters, S.; Gruska, B.; Semtsiv, M.; Chashnikova, M.; Klinkmüller, M.; Fedosenko, O.; Machulik, S.; Aleksandrova, A.; Monastyrskiy, G.; et al. Mid-infrared optical properties of thin films of aluminum oxide, titanium dioxide, silicon dioxide, aluminum nitride, and silicon nitride. *Appl. Opt.* **2012**, *51*, 6789–6798. [CrossRef] [PubMed]
45. Li, Y.; Chernikov, A.; Zhang, X.; Rigosi, A.; Hill, H.M.; van der Zande, A.M.; Chenet, D.A.; Shih, E.; Hone, J.; Heinz, T.F. Measurement of the optical dielectric function of monolayer transition-metal dichalcogenides: MoS_2 , MoSe_2 , WS_2 , and WSe_2 . *Phys. Rev. B Condens. Matter Mater. Phys.* **2014**, *90*, 205422. [CrossRef]
46. Optics.ansys, L. (No Date) Understanding Mesh Order for Overlapping Objects—Ansys Optics, Optics.Ansys. Lumerical. Available online: <https://optics.ansys.com/hc/en-us/articles/360034915233-Understanding-mesh-order-for-overlapping-objects> (accessed on 23 October 2022).
47. Liu, H.; Yang, T.; Chen, J.; Chen, H.; Guo, H.; Saito, R.; Li, M.; Li, L. Temperature-dependent optical constants of monolayer MoS_2 , MoSe_2 , WS_2 , and WSe_2 : Spectroscopic ellipsometry and first-principles calculations. *Sci. Rep.* **2020**, *10*, 15282. [CrossRef] [PubMed]
48. Kim, H.d.; Ohkita, H.; Bente, H.; Ito, S. Photovoltaic Performance of Perovskite Solar Cells with Different Grain Sizes. *Adv. Mat.* **2016**, *28*, 917–922. [CrossRef]
49. Whitfield, P.S.; Herron, N.; Guise, W.E.; Page, K.; Cheng, Y.Q.; Milas, I.; Crawford, M.K. Structures, phase transitions and tricritical behavior of the hybrid perovskite methyl ammonium lead iodide. *Sci. Rep.* **2016**, *6*, 1–16. [CrossRef]
50. Oku, T. Crystal structures of $\text{CH}_3\text{NH}_3\text{PbI}_3$ and related perovskite compounds used for solar cells. *Sol. Cells-New Approaches Rev.* **2015**, *1*, 77–92. [CrossRef]
51. Barrit, D.; Cheng, P.; Tang, M.C.; Wang, K.; Dang, H.; Smilgies, D.M.; Liu, S.; Anthopoulos, T.D.; Zhao, K.; Amassian, A. Impact of the Solvation State of Lead Iodide on Its Two-Step Conversion to MAPbI_3 : An In Situ Investigation. *Adv. Funct. Mater.* **2019**, *29*, 1807544. [CrossRef]

52. Dequilettes, D.W.; Vorpahl, S.M.; Stranks, S.D.; Nagaoka, H.; Eperon, G.E.; Ziffer, M.E.; Snaith, H.J.; Ginger, D.S. Impact of microstructure on local carrier lifetime in perovskite solar cells. *Science* **2015**, *348*, 683–686. [[CrossRef](#)]
53. An, Q.; Paulus, F.; Becker-Koch, D.; Cho, C.; Sun, Q.; Weu, A.; Bitton, S.; Tessler, N.; Vaynzof, Y. Small grains as recombination hot spots in perovskite solar cells. *Matter* **2021**, *4*, 1683–1701. [[CrossRef](#)]
54. Van de Hulst, H.C. *Light Scattering*; Dover Publisher Inc: New York, NY, USA, 1957.
55. Bohren, C.F.; Huffman, D.R. *Absorption and Scattering of Light by Small Particles*; Wiley-Interscience: New York, NY, USA, 1983.
56. Ansys Lumerical, Mie scattering (FDTD). Available online: <https://optics.ansys.com/hc/en-us/articles/360042703433-Mie-scattering-FDTD> (accessed on 8 December 2022).
57. Immanuel, P.N.; Huang, S.-J.; Taank, P.; Goldreich, A.; Prilusky, J.; Byregowda, A.; Carmieli, R.; Zak, A.; Aggarwal, N.; Adarsh, K.V.; et al. *Enhanced Photocatalytic Activity of Cs₄PbBr₆/WS₂ Hybrid Nanocomposite*; ChemRxiv; Cambridge Open Engage: Cambridge, UK, 2022. [[CrossRef](#)]
58. Peimyoo, N.; Shang, J.; Yang, W.; Wang, Y.; Cong, C.; Yu, T. Thermal conductivity determination of suspended mono- and bilayer WS₂ by Raman spectroscopy. *Nanotechnol. Res.* **2015**, *8*, 1210–1221. [[CrossRef](#)]
59. Fang, Q.; Shang, Q.; Zhao, L.; Wang, R.; Zhang, Z.; Yang, P.; Sui, X.; Qiu, X.; Liu, X.; Zhang, Q.; et al. Ultrafast Charge Transfer in Perovskite Nanowire/2D Transition Metal Dichalcogenide Heterostructures. *J. Phy. Chem. Lett.* **2018**, *9*, 1655–1662. [[CrossRef](#)] [[PubMed](#)]
60. Kang, J.; Tongay, S.; Zhou, J.; Li, J.; Wu, J. Band offsets and heterostructures of two-dimensional semiconductors. *Appl. Phys. Lett.* **2013**, *102*, 121111. [[CrossRef](#)]
61. Joe, J.; Yang, H.; Bae, C.; Shin, H. Metal chalcogenides on silicon photocathodes for efficient water splitting: A mini overview. *Catalysts* **2019**, *9*, 149. [[CrossRef](#)]
62. Bahadur, J.; Ghahremani, A.H.; Gupta, S.; Druffel, T.; Sunkara, M.K.; Pal, K. Enhanced moisture stability of MAPbI₃ perovskite solar cells through Barium doping. *Solar Energy* **2019**, *190*, 396–404. [[CrossRef](#)]
63. Behrouznejad, F.; Shahbazi, S.; Taghavinia, N.; Wu, H.-P.; Diau, E.W.-G. A study on utilizing different metals as the back contact of CH₃NH₃PbI₃ perovskite solar cells. *J. Mater. Chem. A* **2016**, *4*, 13488–13498. [[CrossRef](#)]